JBAT 15(1) (2026) 1 – 12

Jurnal Bahan Alam Terbarukan

p-ISSN 2303 0623
e-ISSN 2407 2370

Accredited SINTA 3 by Ministry of Research and Technology/National Research and Innovation Agency
SK No. 10/C/C3/DT.05.00/2025
http://journal.unnes.ac.id/nju/index.php/jbat

Transformation of Biogenic Calcium Carbonate from Waste Eggshells into Hydroxyapatite: A Comparative Study on Crystallographic Characteristics

Agus Jatmiko[1], Rani Nopriyanti[2], Dewi Idamayanti[1], Moch. Wisnu Arif Sektiono[3], Gita Novian Hermana[1,] ✉

DOI: https://doi.org/10.15294/jbat.v15i1.39698

[1]Department of Advanced Materials Engineering, Bandung Polytechnic for Manufacturing, Bandung 40135, West Java, Indonesia.
[2]Department of Manufacture Engineering, Bandung Polytechnic for Manufacturing, Bandung 40135, West Java, Indonesia.
[3]Department of Mechanical Engineering, Politeknik Negeri Malang at PSDKU Campus of Kediri, Kediri, 64114, Indonesia

Article Info

Article history:
Received
22 December 2025
Revised
3 March 2026
Accepted
24 June 2026
Published
June 2026

Keywords:
Crystallite size;
Calcination;
Eggshell waste;
Hydroxiapatite;
Wet chemical precipitation;
X-ray diffraction

Abstract

Hydroxyapatite (HAp) is a calcium phosphate–based biomaterial that has been widely applied in biomedical fields due to its excellent bioactivity and biocompatibility. In this study, HAp was synthesized using a wet chemical precipitation method by utilizing eggshell waste as a calcium source, aiming to develop a sustainable and cost-effective synthesis route. The synthesized products were investigated under two different conditions, namely without calcination and with calcination at 900 °C, in order to evaluate the effect of thermal treatment on the structural and microstructural characteristics of HAp. Phase formation and crystal structure were analyzed using X-ray diffraction (XRD), while surface morphology and elemental composition were examined using scanning electron microscopy (SEM) equipped with energy dispersive spectroscopy (EDS). XRD results confirmed the formation of hydroxyapatite with a hexagonal crystal structure, and calcination treatment led to sharper diffraction peaks, indicating an improvement in crystallinity. SEM observations revealed that the synthesized HAp particles exhibited irregular shapes with a tendency to agglomerate, which is commonly observed in HAp produced via wet chemical precipitation. EDS analysis verified the presence of the main constituent elements, Ca, P, and O, with a Ca/P atomic ratio of 1.67, which is in good agreement with the theoretical stoichiometric value of hydroxyapatite. Crystallite size was evaluated using several XRD-based methods, including the Scherrer, Monshi-Scherrer, Williamson-Hall, Size-Strain Plot, and Halder-Wagner approaches. The calculated crystallite sizes were found to be within the nanometer scale, with variations depending on the assumptions and principles of each method. Overall, the results demonstrate that wet chemical precipitation using eggshell-derived calcium is an effective approach for producing hydroxyapatite with favorable structural and microstructural properties.

INTRODUCTION

Hydroxyapatite (HAp) is a bioactive and biocompatible ceramic material that has been extensively studied for medical applications (Ha et al., 2015), particularly in the fields of orthopedics and dentistry. HAp exhibits a close chemical and structural similarity to human hard tissues, with approximately 70% similarity to bone and up to 90% to dental enamel (Wong et al., 2009). This similarity endows HAp with osteoconductive and bioactive properties, enabling it to support new bone formation and promote osseointegration when applied as an implant or surface coating

✉ Corresponding author:
E-mail: gitanovianh@polman-bandung.ac.id

(Hermana et al., 2024; Lala et al., 2021; Mobarak et al., 2024). HAp can directly bond to the host bone without the formation of an intermediate connective tissue layer, making it highly suitable for applications such as bone defect repair, implant coatings, and filler materials for bone and dental restoration (Mehta & Singh, 2016). Furthermore, owing to its biocompatibility and biodegradability, HAp has also been developed for non-structural applications, including drug and gene delivery systems, as well as antibiotic carriers (Shavandi et al., 2015).

Recent developments indicate that the role of HAp is no longer limited to that of a passive biomaterial, but has evolved into a functional material with tunable physicochemical properties. Advances in synthesis techniques, together with an improved understanding of structure-property relationships, have enabled precise control over the composition, morphology, and surface characteristics of HAp, thereby expanding its potential applications into various technological fields beyond biological contexts (Mondal et al., 2023; Palmer et al., 2008). Nevertheless, Kattimani et al. (2016) emphasized that HAp still suffers from intrinsic limitations, including low mechanical strength, poor fatigue resistance, and thermal instability, which restrict its use, particularly in load-bearing applications. To address these limitations, a wide range of synthesis approaches has been developed, encompassing both solid-state reactions and wet chemical routes such as precipitation and hydrothermal synthesis, with the aim of enhancing the structural and functional performance of HAp. Consequently, the synthesis and engineering of HAp with controlled properties remain a major focus of materials research to date (Dorozhkin, 2017; Liu et al., 2024).

A wide range of HAp synthesis methods has been extensively developed to obtain materials with tailored physicochemical properties for specific applications (Mondal et al., 2023). Among these methods, wet precipitation is one of the most commonly employed approaches, in which calcium and phosphate precursors react in an aqueous medium to form HAp precipitates. Process parameters such as pH, temperature, and reaction time play crucial roles in controlling particle size, morphology, and crystallinity (Hermana et al., 2025; Mobarak et al., 2022; Yelten-Yilmaz & Yilmaz, 2018; Zampieron et al., 2023). The sol-gel method has also been widely adopted due to its ability to produce HAp with homogeneous composition, high porosity, and improved microstructural control through hydrolysis, condensation, and calcination steps (Baladi et al., 2023). In addition, hydrothermal or solvothermal synthesis has been applied to obtain highly crystalline HAp with uniform particle size and morphology through reactions conducted under high-temperature and high-pressure conditions (Goto et al., 2023). Sonochemical approaches utilize ultrasonic waves to accelerate chemical reactions, enabling the formation of HAp nanoparticles with controlled size, shape, and crystallinity (Fu et al., 2018). In recent years, HAp synthesis based on biogenic sources, such as bone, teeth, eggshell waste, and marine organisms, has attracted increasing attention as an environmentally friendly approach capable of producing HAp with diverse morphologies and a wide size range (Wan et al., 2024). Beyond powder synthesis, biomimetic and electrochemical deposition techniques have also been developed to fabricate highly bioactive HAp coatings with structures resembling natural tissues, while allowing precise control over coating thickness, morphology, and composition (Eliaz et al., 2009).

In this study, eggshell waste was utilized as a calcium source for the synthesis of HAp. Previous studies have reported the successful conversion of eggshell-derived calcium into HAp; however, most of these studies primarily focused on phase formation and basic morphological characterization. A systematic investigation of the microstructural evolution, particularly crystallite size analysis using multiple XRD-based calculation approaches, remains relatively limited. Therefore, HAp was synthesized in this work using a wet chemical precipitation method to evaluate the effect of thermal treatment on the structural characteristics of the resulting material. The synthesized products were investigated under two conditions, namely without calcination and with calcination, to examine structural changes induced by heat treatment. The wet chemical precipitation method was selected due to its simplicity, cost-effectiveness, and ability to provide good control over particle formation and chemical composition. Structural characterization was carried out by comparing the crystallographic features of the synthesized HAp under both conditions, with particular emphasis on crystallite size analysis. This analysis aimed to elucidate the microstructural

evolution induced by calcination and its relationship with the crystal growth mechanism of HAp. In addition, several crystallite size calculation methods based on X-ray diffraction data were compared in this study.

MATERIALS AND METHODS

Materials

The primary material used in this study was household chicken eggshells waste, which was utilized as a calcium source for the synthesis of HAp. Deionized water (DI water) obtained from PT. Brataco Indonesia was used as the solvent throughout the synthesis process. Phosphoric acid (H_3PO_4, 85%) was employed as the phosphate source, while ammonium hydroxide (NH_4OH) was used to adjust the pH during the synthesis; both chemicals were purchased from Merck, Germany. All chemicals used were of analytical grade and were utilized as received without any further purification.

Methods

The synthesis process was initiated with a pre-treatment stage of chicken eggshells. Intact eggshells were first washed and boiled in deionized water at 100 °C for 30 minutes to remove impurities and organic contaminants. After boiling, the water was discarded, and the eggshells were dried in an oven at 80 °C.

The dried eggshells were subsequently calcined at 900 °C for 3 hours to produce an active calcium source, during which calcium carbonate ($CaCO_3$) was transformed into calcium oxide (CaO) with the release of carbon dioxide (CO_2). The decomposition reaction of $CaCO_3$ into CaO is expressed in Eq. (1). The calcined product was then ground and sieved to obtain a more uniform particle size distribution.

$$CaCO_{3(s)} \xrightarrow{900\,^{\circ}C} CaO_{(s)} + CO_{2(g)} \quad (1)$$

The CaO powder obtained after the initial calcination was dissolved in 50 mL of deionized water and stirred until homogeneous to produce a 1 M calcium hydroxide [$Ca(OH)_2$] solution. The reaction is described in Eq. (2). Subsequently, a 0.6 M phosphoric acid (H_3PO_4) solution was slowly added to the $Ca(OH)_2$ solution under continuous stirring using a magnetic stirrer. The reaction between $Ca(OH)_2$ and H_3PO_4, as shown in Eq. (3), was carried out at a Ca/P molar ratio of 1.67 under ambient conditions without additional heating. Ammonium hydroxide (NH_4OH) was added to maintain the solution pH at approximately 10 throughout the reaction.

$$CaO_{(s)} + H_2O_{(aq)} \xrightarrow{room\ temperature} Ca(OH)_{2\,(aq)} \quad (2)$$

$$10Ca(OH)_2 + 6H_3PO_4 \xrightarrow{room\ temperature} Ca_{10}(PO_4)_6(OH)_2 + 18H_2O \quad (3)$$

The resulting precipitate was then filtered and thoroughly washed with deionized water to remove residual ions, followed by drying in an oven at 100 °C to eliminate moisture. The obtained HAp powder was divided into two groups: samples without calcination (HAp 0 °C) and samples calcined at 900 °C for 5 hours (HAp 900 °C). A schematic illustration of the synthesis procedure using the wet chemical precipitation method is presented in Figure 1.

Characterizations

Material characterization was performed to evaluate the structural properties, morphology, and chemical composition of the synthesized HAp, including both the non-calcined samples and the samples calcined at 900 °C. Phase identification and crystal structure analysis were carried out using X-ray diffraction (XRD; Bruker D8 Advanced, Germany) with Cu-Kα radiation at a wavelength of 0.15406 nm, a scanning rate of 10°/min, and a step size of 0.02°. The obtained diffraction patterns were matched with the International Center for Diffraction Data (ICDD) database to identify the phases formed. In addition, surface morphology, including particle shape and size, was examined using scanning electron microscopy (SEM; Hitachi SU3500, Japan) operated at an accelerating voltage of 2-3 kV under high vacuum conditions, while elemental composition was analyzed using energy dispersive spectroscopy (EDS) integrated with the SEM system.

Determination of Crystallite Size

In crystalline materials, it is important to distinguish between crystallite size and particle size, as they represent different physical concepts. Crystallite size refers to the dimensions of a single coherently diffracting crystalline domain, whereas particle size may include agglomerates composed of multiple crystallites. In this study, XRD was employed as the primary technique for determining crystallite size due to its effectiveness and reliability

Figure 1. Schematic illustration of the HAp synthesis process using waste eggshell as the calcium precursor.

in analyzing the microstructural characteristics of crystalline materials. The crystallite size of the synthesized hydroxyapatite was determined by analyzing the broadening of diffraction peaks in the XRD patterns. To obtain more comprehensive and accurate results, crystallite size was calculated using several different XRD-based calculation methods.

RESULTS AND DISCUSSION

Morphological Analysis

The surface morphology of the synthesized HAp was examined using SEM to understand the microstructural characteristics of the formed material, as shown in Figure 2. SEM observations reveal that both the non-calcined HAp and the HAp calcined at 900 °C consist of irregularly shaped particles, with plate-like structures predominantly defining the HAp morphology. In addition, a pronounced tendency toward particle agglomeration is observed, leading to the formation of aggregates with relatively rough and porous surfaces. Such agglomeration behavior is commonly reported for HAp powders synthesized via wet chemical precipitation and is associated with high specific surface area and strong interparticle interactions occurring during the precipitation and drying processes. The observed morphological features suggest that the synthesized HAp possesses favorable surface activity, which is relevant for applications involving surface-mediated interactions.

Elemental composition analysis was performed using EDS integrated with the SEM to confirm the presence of the primary constituent elements of HAp. As shown in Figure 3, the EDS spectra exhibit characteristic peaks corresponding to Ca, P, and O, confirming the formation of calcium phosphate compounds. Based on the atomic percentages of Ca and P, the Ca/P ratios of the non-calcined HAp and the HAp calcined at 900 °C were determined to be 2.27 and 1.67, respectively. The calcined HAp sample exhibits a Ca/P ratio consistent with the theoretical stoichiometric value of hydroxyapatite (Ca/P = 1.67). Deviations observed in the Ca/P ratio of the non-calcined HAp are commonly reported for HAp synthesized via wet chemical routes and may be influenced by synthesis parameters such as pH, precursor ratio, and thermal treatment. Overall, the SEM and EDS results confirm that the employed synthesis method successfully produced HAp with characteristic morphology and appropriate elemental composition.

Crystallographic Analysis

The XRD results of the synthesized HAp powder without calcination are presented in Figure 4. The XRD diffraction pattern of the non-calcined HAp shows good agreement with the standard data

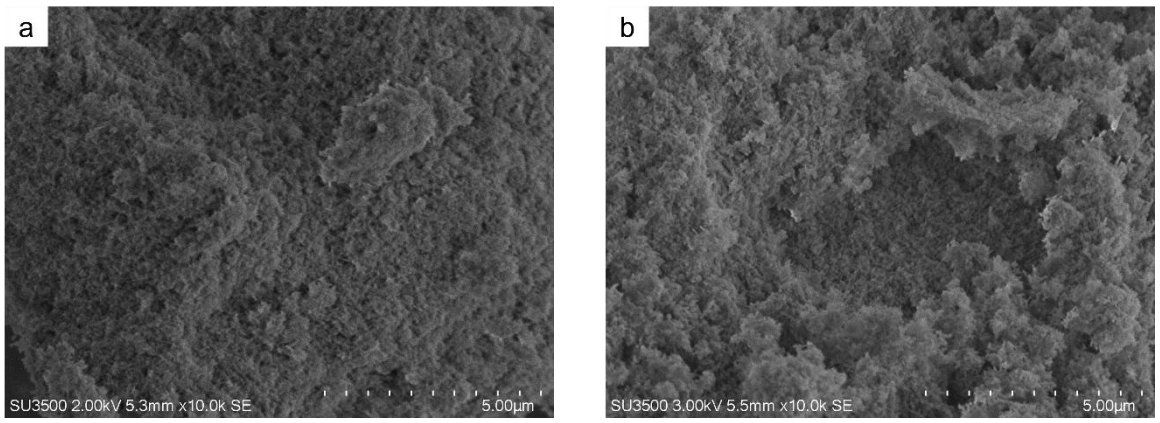

Figure 1. SEM images of synthesized hydroxyapatite (HAp) at calcination temperatures of (a) 0 °C and (b) 900 °C.

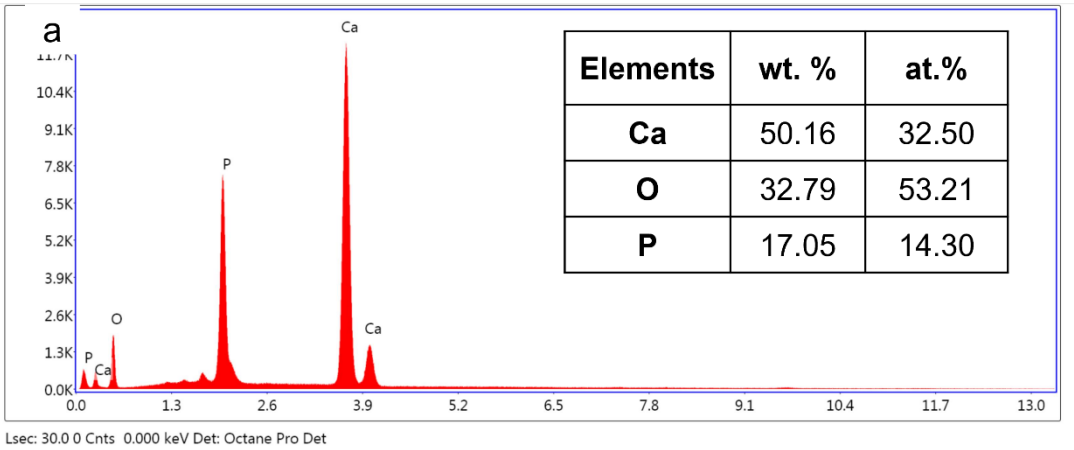

Elements	wt. %	at.%
Ca	50.16	32.50
O	32.79	53.21
P	17.05	14.30

(a)

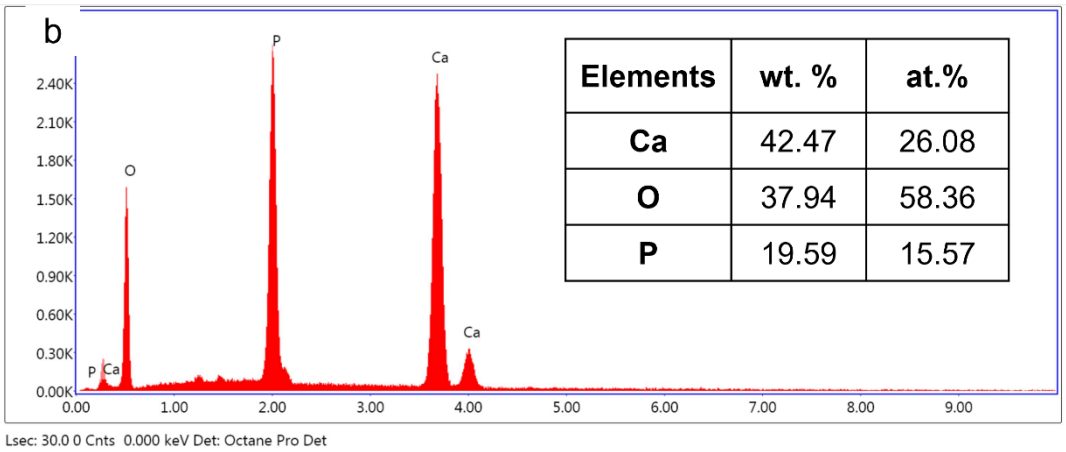

Elements	wt. %	at.%
Ca	42.47	26.08
O	37.94	58.36
P	19.59	15.57

(b)

Figure 2. EDS spectra of synthesized hydroxyapatite (HAp) at calcination temperatures of (a) 0 °C and (b) 900 °C.

from the ICDD for $Ca(OH)_2$ (ICDD card no. #00-044-1481) and HAp (ICDD card no. #00-024-0033). The presence of $Ca(OH)_2$ indicates that a portion of the calcium precursor remained unreacted due to incomplete reaction between Ca^{2+} and the phosphate source during the synthesis process. Therefore, the coexistence of $Ca(OH)_2$ and HAp suggests that the formation of HAp had already occurred, although the reaction had not yet proceeded to completion in the absence of calcination.

Furthermore, the XRD diffraction pattern of the HAp sample calcined at 900 °C exhibits a strong match with the standard ICDD data for hydroxyapatite (ICDD card no. #00-024-0033), indicating the successful formation of the HAp

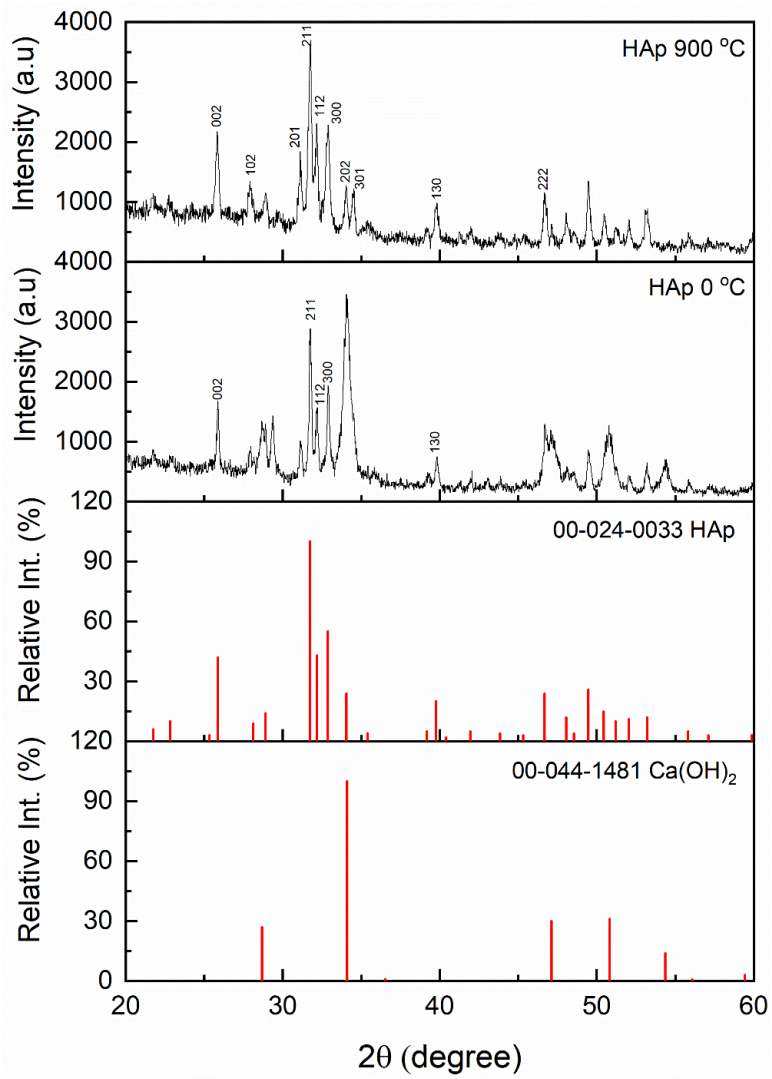

Figure 4. XRD patterns of synthesized HAp at calcination temperatures of 0 °C and 900 °C, compared with the corresponding ICDD reference data.

phase with a hexagonal crystal system. Several characteristic diffraction peaks of HAp, corresponding to the (002), (211), (112), (300), (202), and other crystallographic planes, are clearly identified in the diffraction pattern. The presence of these peaks confirms that a well-defined HAp crystal structure was obtained after the synthesis and thermal treatment.

To obtain more detailed crystallographic information, the lattice parameters of the calcined HAp were calculated based on the interplanar spacing (d) values derived from the XRD data. The calculations were performed using the crystallographic Eq. for a hexagonal crystal system, expressed as shown in Eq. (4).

$$\left(\frac{1}{d}\right)^2 = \frac{4}{3}\left(\frac{h^2 + hk + k^2}{a^2}\right) + \frac{l^2}{c^2} \qquad (4)$$

where d represents the interplanar spacing, a and c are the lattice parameters, and h, k, and l are the Miller indices corresponding to the respective crystallographic planes. The calculated lattice parameter values are summarized in Table 1.

Crystallite Size Calculation

XRD is one of the most reliable techniques for determining crystallite size in both polycrystalline materials and single crystals. Information on crystallite size is obtained through the analysis of diffraction peak broadening observed in XRD patterns. The broadening of diffraction peaks mainly originates from the small crystallite size and lattice microstrain within the crystal structure. In addition, instrumental factors may also contribute to peak broadening. With the advancement of crystallographic studies, various methods have been introduced to estimate

Table 1. Lattice parameters of calcined HAp.

ICDD #00-024-0033		Calcined HAp		hkl
d-spacing (Å)	Intensity (I) (%)	d-spacing (Å)	Intensity (I) (%)	
2.817	100	2.815	100	211
2.779	48	2.780	49.806	112
2.723	72	2.721	56.873	300
a(Å) = b(Å) = 9.432		a(Å) = b(Å) = 9.420		
c(Å) = 6.881		c(Å) = 6.900		

Table 2. Crystallite size calculation using the Scherrer method.

2θ (degree)	***β*** **(radians)**	**L (nm)**	**Average L (nm)**
25.84	0.0037	38.63	
27.92	0.0038	37.21	
28.92	0.0045	31.55	
31.14	0.0034	42.95	
31.76	0.0037	38.60	
32.17	0.0036	39.56	
32.95	0.0048	30.24	
34.06	0.0035	41.96	
34.52	0.0038	38.16	
39.76	0.0049	30.17	
46.69	0.0038	39.33	39.76
48.06	0.0049	31.06	
49.48	0.0031	49.98	
50.47	0.0035	43.91	
52.04	0.0030	52.00	
53.17	0.0031	50.76	
55.89	0.0031	49.96	
59.77	0.0052	30.54	
61.65	0.0047	34.26	
62.98	0.0038	42.35	
64.05	0.0052	31.23	

crystallite size, each based on different assumptions and possessing specific advantages and limitations. Therefore, in this study, several crystallite size calculation approaches based on XRD data were employed to obtain a more representative estimation of the microstructural characteristics of the synthesized HAp.

Scherrer's Method

One of the simplest and most widely used methods for estimating crystallite size based on XRD data is the Scherrer method, which was first introduced by Paul Scherrer (Scherrer, 1918). This method relates crystallite size to the broadening of X-ray diffraction peaks, assuming that the peak broadening is primarily caused by the finite size of coherently diffracting crystal domains. The crystallite size (L) is influenced by the shape factor (K), which is generally close to 0.9 (Stock, 2013), the X-ray wavelength (λ), the diffraction angle (θ), and the full width at half maximum (FWHM, β) of the diffraction peak at the 2θ position. The relationship between these parameters is expressed in Eq. (5).

$$L = \frac{K\lambda}{\beta \cos\theta} \tag{5}$$

In this study, an X-ray wavelength of 0.15406 nm corresponding to Cu-Kα radiation was used. The FWHM values were obtained from the characteristic diffraction peaks of the calcined HAp sample. Based on the calculations using the Scherrer method, the average crystallite size of the calcined HAp was determined to be 39.76 nm. This result indicates that the synthesized HAp is in the nanocrystalline range, which is commonly observed for hydroxyapatite produced via wet chemical synthesis followed by thermal treatment.

Monshi-Scherrer Method

To improve the accuracy of crystallite size determination, Monshi et al. (2012) modified the conventional Scherrer method by applying a logarithmic transformation to its fundamental Eq.. This approach enables a more systematic crystallite size analysis by incorporating multiple diffraction peaks simultaneously. The modified Eq. can be expressed in Eq. (6).

$$\ln\beta = \ln\left(\frac{K\lambda}{L}\right) + \ln\left(\frac{1}{\cos\theta}\right) \tag{6}$$

Using this approach, the values of $\ln\beta$ were plotted against $\ln(1/\cos\theta)$, resulting in a linear relationship. The resulting plot was analyzed using a linear Eq., $y = mx + c$, where the intercept of the fitted line represents $\ln(K\lambda/L)$. Accordingly, the average crystallite size can be directly calculated

from the intercept using the relationship $L = K\lambda/e^{(\text{intercept})}$.

Based on the plot shown in Figure 5, a slope value of −0.64022 and an intercept value of −5.60035 were obtained. Calculation using the intercept value yielded an average crystallite size of 37.51 nm, as summarized in Table 4. The crystallite size obtained using the Monshi–Scherrer method shows good agreement with that calculated using the conventional Scherrer method, thereby reinforcing the reliability of the crystallite size evaluation in this study.

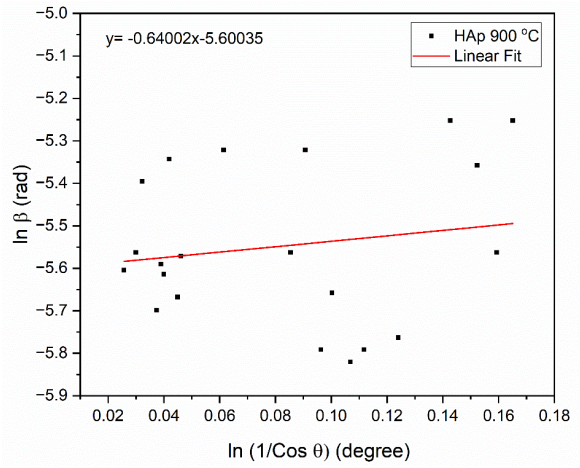

Figure 5. Linear fitting analysis plot of calcined HAp based on the Monshi-Scherrer method.

Williamson-Hall Method

The conventional Scherrer method generally considers only the contribution of crystallite size to diffraction peak broadening, without accounting for lattice microstructural effects such as intrinsic strain (ε), which may arise from point defects, grain boundaries, and stacking faults (Rabiei et al., 2020; Reda et al., 2024). The Williamson-Hall (W-H) method addresses this limitation by incorporating lattice strain into the analysis, recognizing that lattice strain also contributes to X-ray diffraction peak broadening and can be used to estimate crystallite size (Kazi et al., 2020).

In the Williamson-Hall approach, the total diffraction peak broadening (β_{total}) is assumed to be the sum of the contributions from crystallite size (β_{size}) and lattice strain (β_{strain}), as expressed in Eq. (6). The lattice strain resulting from crystal distortion is related to diffraction peak broadening and can be described using Eq. (7) (Mote et al., 2012). By combining the Scherrer Eq. with Eqs. (1), (6), and (7), a linear relationship between peak broadening and diffraction angle is obtained, as given in Eqs. (8) and (9).

$$\beta_{total} = \beta_{size} + \beta_{strain} \quad (6)$$

$$\varepsilon = \frac{\beta_{strain}}{4\tan\theta} \quad (7)$$

$$\beta_{total} = \frac{k\lambda}{L\cos\theta} + 4\varepsilon\tan\theta \quad (8)$$

$$\beta_{total}\cdot\cos\theta = \frac{k\lambda}{L} + 4\varepsilon\sin\theta \quad (9)$$

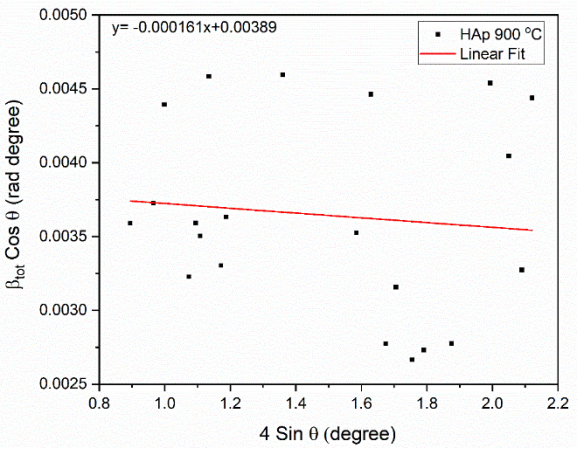

Figure 6. Linear fitting analysis plot of calcined HAp based on the Williamson–Hall method.

Eq. (9) is known as the uniform deformation model (UDM), which assumes that strain is isotropically distributed throughout the crystal lattice. In this study, the UDM analysis was performed by plotting $\beta_{\text{total}}\cos\theta$ against $4\sin\theta$, as shown in Figure 6. Linear fitting of the plot yielded a slope value of −0.000161 and an intercept value of 0.00389. The intercept corresponds to the parameter $K\lambda/L$; therefore, the average crystallite size calculated using the Williamson–Hall method was 35.64 nm, as summarized in Table 3.

Size-Strain Plot Method

The Williamson–Hall method is based on the assumption that crystallite diffraction domains are isotropic, such that diffraction peak broadening is considered to be uniform in all directions (Balzar & Ledbetter, 1993). This approach correlates peak broadening with the diffraction angle to evaluate the contributions of crystallite size and lattice strain. However, to improve the accuracy of diffraction peak broadening analysis, particularly at low diffraction angles, the size–strain plot (SSP) method was developed. The SSP method separates the total

peak broadening into two main components: broadening caused by crystallite size, which is represented by a Lorentzian function (β_L), and broadening resulting from lattice strain, which is described by a Gaussian function (β_G). This relationship can be generally expressed by Eq. (10).

$$\beta = \beta_L + \beta_G \quad (10)$$

The SSP method is specifically designed for analyzing crystalline materials with relatively uniform structures in all directions and is known to provide higher precision, particularly for diffraction peaks at low angles (Kafashan, 2018). The mathematical relationship between crystallite size and lattice strain in this approach is expressed by Eq. (11) (Basak et al., 2022; Nath et al., 2020; Prabhu et al., 2014). In this study, the XRD data were analyzed by plotting $(d \cdot \beta \cdot \cos\theta)^2$against $(d^2 \cdot \beta \cdot \cos\theta)$, resulting in a linear relationship, as shown in Figure 6. The crystallite size was then calculated from the slope of the linear fitting, which corresponds to the parameter $k\lambda/L$. Based on this analysis, the average crystallite size obtained using the SSP method was 316.54 nm, as summarized in Table 3.

$$(d \cdot \beta \cdot \cos\theta)^2 = \frac{k\lambda}{L} \cdot (d^2 \cdot \beta \cdot \cos\theta) + \frac{\varepsilon^2}{4} \quad (11)$$

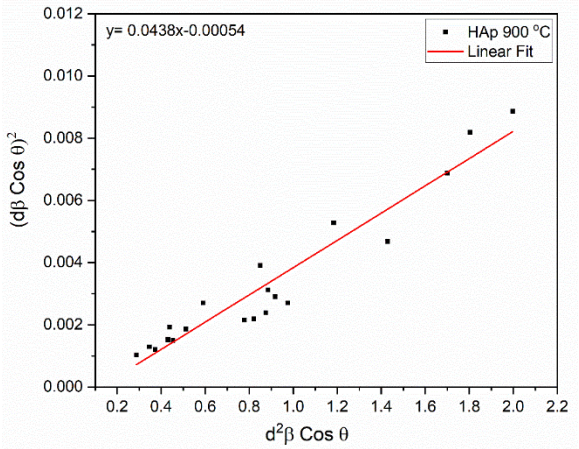

Figure 7. Linear fitting analysis plot of calcined HAp based on the size-strain plot (SSP) method.

Halder-Wagner Method

The Halder-Wagner method (HWM) was developed based on the consideration that X-ray diffraction peak broadening in crystalline materials does not strictly follow either a pure Lorentzian or Gaussian function (Halder & Wagner, 1966; Hepp & Baerlocher, 1988). Instead, the XRD peak profile is more appropriately described by a symmetric Voigt function, which represents a convolution of both Lorentzian and Gaussian functions (Halder & Wagner, 1966; Motevalizadeh et al., 2014). Accordingly, the HWM was introduced to accommodate a more realistic description of peak broadening behavior, particularly at low to intermediate diffraction angles where peak overlap is relatively minimal.

In the HWM approach, diffraction peak broadening is expressed as a combined contribution of the Lorentzian and Gaussian components, as formulated in Eq. (12), where β_L and β_G represent the FWHM of the Lorentzian and Gaussian functions, respectively. The main advantage of this method over other approaches lies in its enhanced sensitivity to diffraction peaks at low and intermediate angles, enabling a more accurate estimation of crystallite size. The mathematical formulation of the Halder–Wagner method is further expressed in Eq. (13), with supporting parameters defined in Eqs. (14) and (15). By combining and rearranging these Eqs., a linear relationship is obtained, as shown in Eq. (16).

$$\beta_{hkl}^2 = \beta_L \times \beta_{hkl} + \beta_G^2 \quad (12)$$

In this study, the HWM analysis was performed by plotting $\frac{\beta \cos\theta}{\sin^2\theta}$ as the x-axis and $\left(\frac{\beta}{\tan\theta}\right)^2$ as the y-axis, as illustrated in Figure 8. Linear fitting of the plot yielded a slope value of 0.04738, which corresponds to the parameter $K\lambda/D$. Based on this relationship, the crystallite size calculated using the Halder–Wagner method was approximately 20.91 nm, as summarized in Table 3. In addition, the fitting resulted in an intercept value of -0.05544, which is mathematically related to the lattice strain parameter. However, since the obtained intercept value is negative, a valid calculation of lattice strain could not be performed using the HWM in this study.

$$\left(\frac{\beta^*}{d^*}\right)^2 = \frac{K\beta^*}{D(d^*)^2} + (2\varepsilon)^2 \quad (13)$$

$$\beta^* = \frac{\beta \cos\theta}{\lambda} \quad (14)$$

$$d^* = \frac{2d \sin\theta}{\lambda} \quad (15)$$

$$\left(\frac{\beta}{\tan\theta}\right)^2 = \frac{K\lambda}{D}\frac{\beta\cos\theta}{\sin^2\theta} + 16\varepsilon^2 \qquad (16)$$

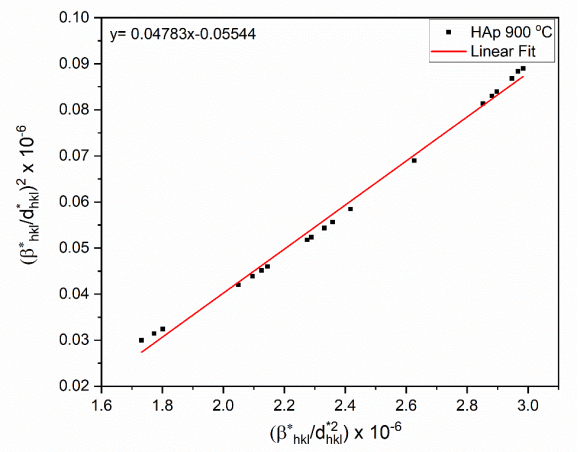

Figure 8. Linear fitting analysis plot of calcined HAp based on the Halder-Wagner method.

Table 3. Comparison of crystallite size calculated using different methods.

No.	Method	Crystallite Size (nm)
1	Scherrer's method	39.76
2	Monshi Scherrer method	37.51
3	Williamson-Hall method	35.64
4	Size-strain plot method	316.54
5	Halder-Wagner method	20.91

CONCLUSIONS

HAp was successfully synthesized using a wet chemical precipitation method by utilizing eggshell waste as a calcium source. XRD analysis confirmed the successful formation of the HAp phase. SEM results revealed irregularly shaped particles with a tendency toward agglomeration, while EDS analysis confirmed the presence of Ca, P, and O elements, with a Ca/P ratio of 1.67, which is consistent with the theoretical value for samples calcined at 900 °C. Crystallite size analysis based on XRD using various calculation methods indicated that the synthesized HAp exhibited nanocrystalline characteristics, with crystallite sizes ranging from 20.91 to 316.54 nm, depending on the assumptions of each calculation method. Overall, the results demonstrate that the wet chemical precipitation approach using eggshell-derived calcium is an effective method for producing hydroxyapatite with controlled structural and microstructural properties. However, further studies are required to optimize synthesis parameters to better control particle morphology, reduce agglomeration, and improve crystallinity.

ACKNOWLEDGEMENTS

This research was supported by Bandung Polytechnic for Manufacturing under grant number 0203/PL11/KD/2025.

REFERENCES

Baladi, M., Amiri, M., Mohammadi, P., Mahdi, K. S., Golshani, Z., Razavi, R., Salavati-Niasari, M. 2023. Green sol–gel synthesis of hydroxyapatite nanoparticles using lemon extract as capping agent and investigation of its anticancer activity against human cancer cell lines (T98, and SHSY5). Arabian Journal of Chemistry. 16(4): 104646.

Balzar, D., Ledbetter, H. 1993. Voigt-function modeling in Fourier analysis of size-and strain-broadened X-ray diffraction peaks. Applied Crystallography. 26(1): 97-103.

Basak, M., Rahman, M. L., Ahmed, M. F., Biswas, B., Sharmin, N. 2022. The use of X-ray diffraction peak profile analysis to determine the structural parameters of cobalt ferrite nanoparticles using Debye-Scherrer, Williamson-Hall, Halder-Wagner and Size-strain plot: Different precipitating agent approach. Journal of Alloys and Compounds. 895: 162694.

Dorozhkin, S. 2017. Calcium orthophosphates ($CaPO_4$): Occurrence and properties. Morphologie. 101(334): 125-142.

Eliaz, N., Shmueli, S., Shur, I., Benayahu, D., Aronov, D., Rosenman, G. 2009. The effect of surface treatment on the surface texture and contact angle of electrochemically deposited hydroxyapatite coating and on its interaction with bone-forming cells. Acta biomaterialia. 5(8): 3178-3191.

Fu, L.-H., Qi, C., Liu, Y.-J., Cao, W.-T., Ma, M.-G. 2018. Sonochemical synthesis of cellulose/hydroxyapatite nanocomposites and their application in protein adsorption. Scientific reports. 8(1): 8292.

Goto, T., Yin, S., Asakura, Y., Cho, S. H., Sekino, T. 2023. Simultaneous synthesis of hydroxyapatite fibres and β-tricalcium phosphate particles via a water controlled-release solvothermal process. CrystEngComm. 25(14): 2021-2026.

Ha, S.-W., Jang, H. L., Nam, K. T., Beck Jr, G. R. 2015. Nano-hydroxyapatite modulates osteoblast lineage commitment by stimulation of DNA methylation and regulation of gene expression. Biomaterials. 65. 32-42.

Halder, N., Wagner, C. 1966. Separation of particle size and lattice strain in integral breadth measurements. Acta Crystallographica. 20(2): 312-313.

Hepp, A., Baerlocher, C. 1988. Learned peak shape functions for powder diffraction data. Australian Journal of Physics. 41(2): 229-236.

Hermana, G. N., Nugraha, D. K., Nadi, M. R. G., Sektiono, M. W. A., Mayello, R. M., Farhan, M., Rizqi, F. M. 2024. Surface Evaluation of Tricalcium Phosphate Bioceramic Coating on SS-316L by Electrophoretic Deposition. Jurnal Bahan Alam Terbarukan. 13(1): 38-47.

Hermana, G. N., Siswanto, A., Jatmiko, A., Mayello, R. M., Kusuma, N. C. 2025. Utilization of natural limestone in the development of hydroxiapatite: A comparative approach on crystallographic parameters. MRS Advances. 10: 1723 - 1729.

Kafashan, H. 2018. Structural characterizations of pure SnS and In-doped SnS thin films using isotropic and anisotropic models. Materials Research Express. 5(4): 046417.

Kattimani, V. S., Kondaka, S., Lingamaneni, K. P. 2016. Hydroxyapatite–-Past, present, and future in bone regeneration. Bone and Tissue Regeneration Insights. 7: S36138.

Kazi, S., Savanur, F., Kakati, S., Mathad, S. N., Jeergal, P., Pujar, A., Pujar, R. 2020. Sintering temperature dependent structural and mechanical studies of BaxPb1− xTiO3 ferroelectrics. Journal of Nano- and Electronic Physics. 12(4): 04018-1-04018-5.

Lala, S. D., Barua, E., Deb, P., Deoghare, A. B. 2021. Physico-chemical and biological behaviour of eggshell bio-waste derived nano-hydroxyapatite matured at different aging time. Materials Today Communications. 27. 102443.

Liu, C., Xu, M., Wang, Y., Yin, Q., Hu, J., Chen, H., Zhou, W. 2024. Exploring the potential of hydroxyapatite-based materials in biomedicine: A comprehensive review. Materials Science and Engineering: R: Reports. 161. 100870.

Mehta, M. S., Singh, R. P. 2016. Effects of aging time and sintering temperatures on thermal, structural and morphological properties of coralline hydroxyapatite. Journal of Nuclear Physics Material Sciences Radiation and Applications. 3(2): 223-237

Mobarak, M. B., Hossain, M. S., Yeasmin, Z., Mahmud, M., Rahman, M. M., Sultana, S., Ahmed, S. 2022. Probing the photocatalytic competency of hydroxyapatite synthesized by solid state and wet chemical precipitation method. Journal of Molecular Structure. 1252: 132142.

Mobarak, M. B., Uddin, M. N., Chowdhury, F., Hossain, M. S., Mahmud, M., Sarkar, S., Ahmed, S. 2024. Solid-state synthesis of poultry waste derived hydroxyapatite: Effect of calcination temperature on crystallographic parameters and biomedical competency. Journal of Molecular Structure. 1301: 137321.

Mondal, S., Park, S., Choi, J., Vu, T. T. H., Doan, V. H. M., Vo, T. T., Oh, J. 2023. Hydroxyapatite: A journey from biomaterials to advanced functional materials. Advances in colloid and interface science. 321: 103013.

Monshi, A., Foroughi, M. R., Monshi, M. R. 2012. Modified Scherrer equation to estimate more accurately nano-crystallite size using XRD. World journal of nano science and engineering. 2(3): 154-160.

Mote, V. D., Purushotham, Y., Dole, B. 2012. Williamson-Hall analysis in estimation of lattice strain in nanometer-sized ZnO particles. Journal of theoretical and applied physics. 6(1): 6.

Motevalizadeh, L., Heidary, Z., Abrishami, M. E. 2014. Facile template-free hydrothermal synthesis and microstrain measurement of

ZnO nanorods. Bulletin of materials science. 37(3): 397-405.

Nath, D., Singh, F., Das, R. 2020. X-ray diffraction analysis by Williamson-Hall, Halder-Wagner and size-strain plot methods of CdSe nanoparticles-a comparative study. Materials Chemistry and Physics. 239: 122021.

Palmer, L. C., Newcomb, C. J., Kaltz, S. R., Spoerke, E. D., Stupp, S. I. 2008. Biomimetic systems for hydroxyapatite mineralization inspired by bone and enamel. Chemical reviews. 108(11): 4754-4783.

Prabhu, Y. T., Rao, K. V., Kumar, V. S. S., Kumari, B. S. (2014). X-ray analysis by Williamson-Hall and size-strain plot methods of ZnO nanoparticles with fuel variation. World journal of nano science and engineering. 4(1):21-28

Rabiei, M., Palevicius, A., Monshi, A., Nasiri, S., Vilkauskas, A., Janusas, G. 2020. Comparing methods for calculating nano crystal size of natural hydroxyapatite using X-ray diffraction. Nanomaterials. 10(9): 1627.

Reda, M., Ateia, E. E., El-Dek, S., Arman, M. 2024. New insights into optical properties, and applications of Zr-doped BaTiO3. Applied Physics A. 130(4): 240.

Scherrer, P. 1918. Estimation of the size and internal structure of colloidal particles by means of röntgen. Nachrichten von der Gesellschaft der Wissenschaften zu Göttingen. *2*: 96-100.

Shavandi, A., Bekhit, A. E.-D. A., Ali, A., Sun, Z. 2015. Synthesis of nano-hydroxyapatite (nHA) from waste mussel shells using a rapid microwave method. Materials Chemistry and Physics. 149: 607-616.

Stock, S. 2013. Elements of X-ray diffraction: pearson new international edition PDF eBook: Pearson Higher Ed.

Wan, L., Cui, B., Wang, L. 2024. A review on preparation raw materials, synthesis methods, and modifications of hydroxyapatite as well as their environmental applications. Sustainable Chemistry and Pharmacy. 38: 101447.

Wong, K., Wong, C., Liu, W., Pan, H., Fong, M., Lam, W., Luk, K. 2009. Mechanical properties and in vitro response of strontium-containing hydroxyapatite/polyetheretherketone composites. Biomaterials. 30(23-24): 3810-3817.

Yelten-Yilmaz, A., Yilmaz, S. 2018. Wet chemical precipitation synthesis of hydroxyapatite (HA) powders. Ceramics International. 44(8): 9703-9710.

Zampieron, C. I., Cesca, K., Faita, F. L., Immich, A. P. S., Parize, A. L. 2023. Effect of heat-treatment temperature on the structure of calcium phosphate synthesized by wet precipitation. Ceramics International. 49(17): 29198-29207.